with that of Bethe and Longmire. The latter agrees better with the weighted average of the measurements at 2.76 Mev, which has a higher accuracy. The results of Halpern and Woodward[7] are difficult to fit to either curve. It is evident that one should try to obtain at energies of 2.504 and 2.618 Mev results with the same precision as that already obtained for 2.76 Mev. It is unlikely that the final curve of the ratio σ_m/σ_e against energy will lie significantly above the Bethe-Longmire curve. Although the experimental ratio σ_m/σ_e is not in contradiction with the Bethe-Longmire theory, it should be noted that the experimental total cross section[10] $\sigma_r=\sigma_m+\sigma_e$ lies well above the theoretical values.

The authors would like to express their gratitude to Mr. R. West, Isotope Division, A.E.R.E. Harwell, for arranging the special irradiations; to Mr. V. Round for his ideas and for construction of the source and toroid assembly; to the Iodine Educational Bureau for the gift of some ethyl iodide; and to Lord Cherwell for extending to us the facilities of his laboratory. We are very grateful to Professor L. Hulthén for his guidance on several occasions.

---

[10] G. R. Bishop, C. H. Collie, H. Halban, A. Hedgsarv, K. Siegbahn, S. DuToit, and R. Wilson, Phys. Rev. **80**, 211 (1950).

PHYSICAL REVIEW VOLUME 81, NUMBER 2 JANUARY 15, 1951

Fine Structure of the Hydrogen Atom.* Part II

Willis E. Lamb, Jr., and Robert C. Retherford†
Columbia Radiation Laboratory, Columbia University, New York, New York

(Received September 29, 1950)

In the first paper of this series, the shift of the $2^2S_{\frac{1}{2}}$ level of hydrogen was determined to be 1000 Mc/sec. A new apparatus differing from the original one in details, but not in principle, has been built in order to improve the accuracy of the above result. This provides a greater yield of metastable hydrogen atoms, a more homogeneous magnetic field, and more accurate means of measurement of magnetic field and frequency. With these improvements, preliminary measurements of considerably increased accuracy have been made on both hydrogen and deuterium. The transitions observed were $2^2S_{\frac{1}{2}}$, $m=\frac{1}{2}$, to $2^2S_{\frac{1}{2}}$, $m=-\frac{1}{2}$, as well as to $2^2P_{\frac{1}{2}}$, $m=\frac{1}{2}$ and $m=-\frac{1}{2}$. The first transition permits observation of the hyperfine structure of $2^2S_{\frac{1}{2}}$, as well as an accurate calibration of magnetic field. Hyperfine structure was also resolved for the last transition in hydrogen. There was no observable difference between the level shifts for hydrogen and deuterium which may be taken as 1062±5 Mc/sec. Later papers of this series will deal with the numerous experimental and theoretical corrections necessary to obtain a level shift accurate to 1 Mc/sec.

F. NEW APPARATUS

32. Introduction

THE apparatus described[59] in Part I was improvised during the exploratory work necessary to establish the formation and detection of metastable hydrogen atoms. It was geometrically inconvenient and not well suited for precise measurements. In addition, the magnetic field was found to be excessively inhomogeneous, the magnet too small, and the pumping speed inadequate, and no cold traps were provided.

A second apparatus has been built with extensive improvements in the above respects, and in the auxiliary equipment relating to magnetic field, radiofrequency, and power, etc. With this, it has been possible to obtain results having an internal consistency close to 1 Mc/sec. In order to determine the relative positions of the $2^2S_{\frac{1}{2}}$, $2^2P_{\frac{1}{2}}$, and $2\,^2P_{\frac{3}{2}}$ levels, however, it is necessary to apply many experimental and theoretical corrections to the raw data. Fortunately, it is possible to establish empirically that these corrections can lead to a change of only a few megacycles per second in the results. In this paper, accordingly, we will give an account of the work up to about a year ago, when it was possible to quote a result[60] with a limit of error of ±5 Mc/sec. It is planned to devote Part III of this series to a discussion of the corrections and Part IV to a determination of the precise level shifts from the data.

33. General Features

A cross section of the apparatus in a horizontal plane is shown in Fig. 27 and has the same general features as those shown in Fig. 19 of Part I. Source of atomic hydrogen *a*, electron bombarder *c*, *d*, *e* and detector *j*, *k* are now in separately pumped chambers. The source chamber is pumped by the main pump (DPI-MC 275) and the other chambers by differential pumps (DPI-GF 20W) emptying into the source chamber. There is a

---

* Work supported jointly by the Signal Corps and ONR.

† Present address: Department of Electrical Engineering, University of Wisconsin, Madison, Wisconsin.

[59] Part I of this series appeared in Phys. Rev. **79**, 549 (1950). Frequent references to this paper are made. Sections, figures, equations, and footnotes of Part II are numbered consecutively after those of Part I. The designation of states by letters α, β, *a*, *b*, *c*, *d*, *e*, *f* is explained in Fig. 14.

[60] R. C. Retherford and W. E. Lamb, Jr., Phys. Rev. **75**, 1325 (1949).

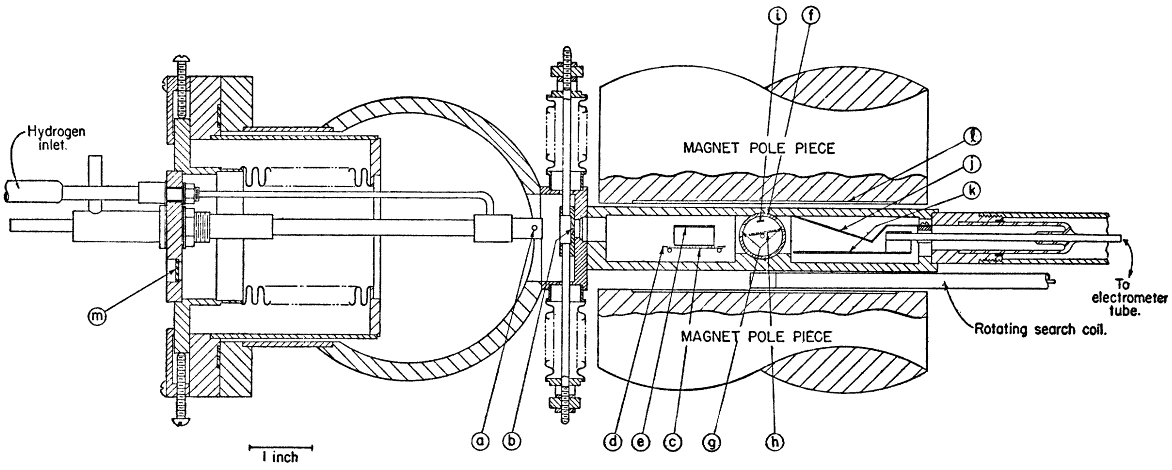

FIG. 27. Cross section of second apparatus: (*a*) tungsten oven of hydrogen dissociator, (*b*) movable slits, (*c*) electron bombarder cathode, (*d*) grid, (*e*) anode, (*f*) transmission line, (*g*) slots for passage of metastable atoms through interaction space, (*h*) plate attached to center conductor of r-f transmission line, (*i*) dc quenching electrode, (*j*) target for metastable atoms, (*k*) collector for electrons ejected from target, (*l*) pole face of magnet, (*m*) window for observation of tungsten oven temperature.

liquid nitrogen trap and baffle between each pump and chamber. The source and electron bombarder chambers are separated by slits *b*, and the electron bombarder and detector chambers by slots *g* in the rf line. The pumps are backed by a booster pump (DPI-MB 100) and by a Kinney (CVD 556) mechanical pump. Ionization gauges are mounted on the source and detector chambers; and, in addition, a Knudsen gauge (DPI-BL 1) is mounted on the source chamber. During operation the detector chamber pressure is monitored by the ionization gauge and the source chamber pressure by the Knudsen gauge. The latter pressure gives an indication of the hydrogen flow.

The electron bombarder and detector chamber and rf line are situated in a rectangular parallelopiped which fits into the magnet gap. The GF-20W pump leads come in at the bottom of this body.

Gas is admitted to the system directly from a hydrogen or deuterium tank through a reducing valve, a hot palladium tube, and a variable leak of the type described by Nier, Ney, and Inghram.[61]

The bellows allow the position of the source *a* to be adjusted for optimum signal strength and the separating slit *b* is adjustable in width and position. The rf line can be rotated to select the best angle of the slits.

34. Hydrogen Dissociator

Hydrogen atoms are produced by thermal dissociation as in Part I, and the dissociator (Fig. 28) is very similar to that shown in Fig. 20. Certain modifications have been made to obtain greater life. A separate lead for hydrogen reduces the chance of leaks at brazed joints in contact with cooling water. A heavy piece of copper was interposed between the molybdenum end and the stainless steel tube, and the size of the molybdenum was increased to $\frac{3}{8}$-in diameter stock to improve cooling.

The tungsten tube is now made from a solid rod by grinding off half of an 0.063-in. diameter rod, grinding a 1/64×1/64-in. groove down its length, and then putting two of these pieces together. A small slit is ground on one side of each piece in the cleavage plane to serve as an exit for the atoms as illustrated in the detail of Fig. 28. This tungsten tube is very much more rugged than the previous type, and usually lasts for several months of laboratory usage at a temperature of 2500°–2600°K. When properly constructed, the two halves of the tungsten tube weld together after a short time and form a true tube. Typical operating conditions are 2.31 v, 188 am, 2520°K. The power is supplied from a large transformer and a Sorensen voltage regulator.

35. Electron Bombarder

At the time this apparatus was designed, it was hoped that most of the electron bombarder troubles previously encountered, especially with the oxide-coated cathode, would be cured by the greatly increased pumping speed. Although there was some improvement, the difficulty with emission poisoning persisted, and the life of a cathode was only a few days with uninterrupted operation of all pumps. This situation was vastly improved by redesigning the electron bombarder with a tungsten wire cathode. No more trouble was encountered with emission poisoning. Despite the great reduction in emitting area, the observed signal was much more stable and ample for our purposes, except under conditions to be described in Sec. 43.

A cross section of the present electron bombarder in a horizontal plane through the filament is shown in Fig. 27 (*d*, *e*, and *c*) and an enlarged cross section in a vertical plane parallel to the magnetic field lines is

---

[61] Nier, Ney, and Inghram, Rev. Sci. Instr. **18**, 191 (1947).

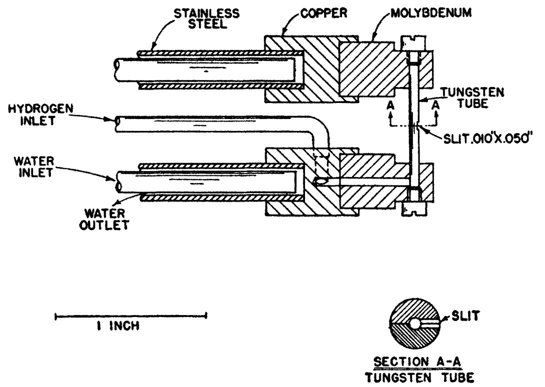

FIG. 28. Detail of end of hydrogen dissociator.

shown in Fig. 29. The filament is 0.010-in. diameter tungsten wire mounted in such a way that it is under tension at all operating temperatures. The grid wires are 0.004-in. diameter tungsten, 67 per inch, and are held at one end only to prevent buckling. The taut filament and nonbuckling grid wires permit very stable operation of the electron bombarder although the grid-filament spacing is 0.010-in. or less. This small spacing permits the control of the anode current by varying the filament temperature without encountering space charge limitation. The anode has the shape of a U and is designed to reduce depression of the potential in the region occupied by electrons. It is made of molybdenum sheet and has a width of about $\frac{5}{8}$ in., a depth of $\frac{5}{16}$ in. and a height of 0.050 in i.d.

On account of the magnetic field, the thickness of the electron beam is effectively the filament diameter, or only slightly larger. The width of the electron beam is equal to the emitting length of the filament or about a centimeter. A very adequate and helpful theory for the behavior of a thin electron beam in a metallic enclosure of this sort has been given by Haeff.[62] Heaters (not shown in the figures) are installed on the top and bottom of the anode for cleaning it while in the apparatus.

The grid is operated at ground potential, the filament at −10.8 v (7 dry cells) to center tap, while the anode is connected to the grid through a microammeter. The filament is operated on 60-cy ac with a filament voltage drop of about 1.7 v rms at ordinary operating conditions. A Sorensen voltage regulator supplies the power.

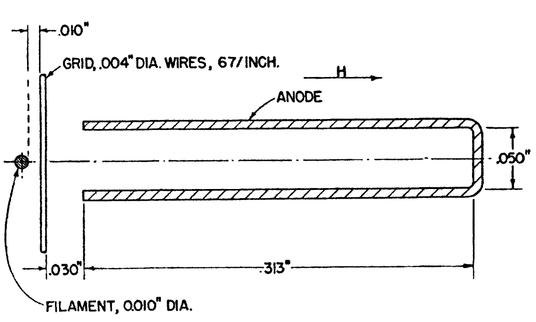

FIG. 29. Cross section of electron bombarder in plane at right angles to beam of hydrogen atoms. The U-shaped anode greatly reduces space charge in the electron beam.

36. rf and dc Quenching Region

A coaxial transmission line is chosen as the most versatile type of region for interaction of the metastable atoms with the rf field. The uncertainty principle broadening of the resonances is made negligible by increasing the time spent by metastable atoms in the rf field. The line is enlarged in the interaction space, and a piece of molybdenum sheet is welded to the center conductor to make the reciprocal time of transit less than 10^6 sec^{-1}. Transitions induced by a perpendicular component of rf electric field are thereby reduced in intensity, but can still be studied, although less favorably, as there are appreciable fringing field components in the required direction. The stream of atoms passes through slits, *g*, between inner and outer conductors. The transmission line enters at the top of the apparatus and terminates at the bottom in an unmatched crystal load whose current is used to monitor the rf power. Although this arrangement has great versatility, it has the disadvantage of making it difficult to estimate the rf fields and requiring excessive rf power because of mismatch at the interaction space and at the crystal.

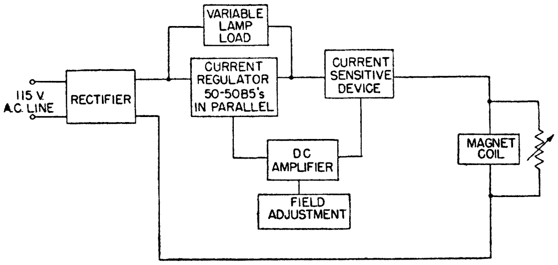

FIG. 30. Block diagram for magnet current stabilizing circuit.

An auxiliary electrode, *i*, is placed in the interaction region to permit quenching of the metastable atoms by electrostatic fields without breaking the rf circuit. A dc voltage is applied between this electrode and the outer conductor. A potential difference of 125 v suffices to quench essentially all of the metastable atoms at the magnetic fields used here. The corresponding change in electrometer current can be used to monitor the total signal due to metastable atoms.

37. Detector

The detector consisting of tungsten target *j* and collector *k* of Fig. 27 differs from that used in the previous apparatus only in nonessential details of construction. The electrometer circuit was changed from balanced to unbalanced type without increased drift or instability. A considerable reduction in galvanometer

---

[62] A. V. Haeff, Proc. Inst. Elec. Engrs. 27, 586 (1939).

fluctuation was obtained by evacuating the vessel containing the FP54 tube and grid circuit. The input resistance used was about 7×10^{10} ohms and the over-all current sensitivity about 1.9×10^{-16} amp/mm with fluctuations of about 1 mm.

38. Magnet

An electromagnet with pole pieces $5\frac{1}{2}$ in. in diameter is used. The pole pieces and yoke are constructed of an electromagnet iron of the type used in the Nevis cyclotron. To make the field more homogeneous, the pole pieces are cut away as shown in Fig. 27. At a field of 1000 gauss, the field is uniform throughout the interaction space to better than $\frac{1}{6}$ gauss.

A circuit illustrated in block diagrams in Fig. 30 controls and stabilizes the magnet current. This is patterned after a similar system devised by Lentz[63] and Katz. The current sensitive device which furnishes the error signal to the dc amplifier is a G.E. 2B23 magnetically controlled diode placed in a solenoid which is energized by the magnet current. A ten-turn helically wound L & N potentiometer is used to adjust the magnetic field. Aside from quite manageable thermal drifts, this circuit holds the magnetic field current steady to one part in fifty thousand.

39. Magnetic Field Measurement

Determination of the level shifts requires knowledge of the magnetic fields used in taking resonance curves. The slopes of the frequency *versus* field curves αe and αf of Fig. 15 are about one and two megacycles per gauss respectively. Consequently, a determination of the level shift to an accuracy of 1 Mc/sec requires an absolute measurement of the magnetic field to an accuracy of 1 or $\frac{1}{2}$ gauss, respectively.

It would have been possible to make such measurements by observing nuclear induction effects in the interaction space; but this would not have been convenient because of the range of magnetic fields, from nearly zero to 4000 gauss, to be covered. Instead, a rotating search coil method was devised which serves this purpose adequately. An hysteresis-type synchronous motor drives two search coils at 30 cps, one in the field of a permanent magnet for a comparison signal and the other in the magnetic field to be measured (Fig. 31). The permanent magnet is mounted inside an iron shield on the motor supporting structure. Search coil No. 2 is shown in position in Fig. 27. The coils have an NA of about 150 cm^2, and fit in a cylinder with an over-all diameter of $\frac{1}{4}$ in. Signals from the search coils are picked up with graphalloy brushes from coil silver slip rings. Three brushes 120° apart are used on each slip ring to minimize brush noise with the brush bearing area adjusted to give low noise. Figure 31 shows the measuring circuit. The 30-cps amplifier has a gain of about 5000 and a band width of 5 cy, and is of a design suggested by J. Lentz.[64] The coils are connected so that there is a circulating current at balance which is obtained by observing a Lissajous figure on an oscilloscope. The connection from R_1 to the oscilloscope supplies the horizontal signal required for producing the Lissajous figure. At balance

$$R_2/R_1=\omega(NA)_2H_2/[\omega(NA)_1H_1], \tag{96}$$

or

$$H_2=\text{const}\times R_2. \tag{96a}$$

R_1 and R_2 are G.R. 5-decade resistance boxes and in Eqs. (96) include the lead and search coil resistances. For best results, the relative phase of the signals must be carefully adjusted. This is done by rotation of one of the shafts relative to the other, and requires an adjustment to about 10^{-4} radian.

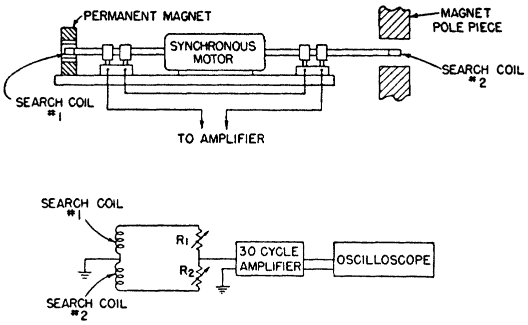

FIG. 31. Apparatus for measurement of magnetic field.

This method has the advantage of independence of line frequency and stability of relative phase, and it is easily possible to make relative field measurements at a field of 1000 gauss to an accuracy of 1/50 gauss. If two separate motors are used, small erratic relative changes in phase give a great deal of trouble.

In order to make absolute field measurements, it is necessary to have a determination of the constant in Eq. (96a). This can conveniently be obtained from an observation of the sharp transitions $\alpha\beta$ discussed in Sec. 44. Except for small corrections, such as that due to motional Stark effect and incomplete Back-Goudsmit effect of hyperfine structure, the frequency required for this transition is given by the equation

$$h\nu=2(1+\alpha/2\pi)\mu_0H, \tag{97}$$

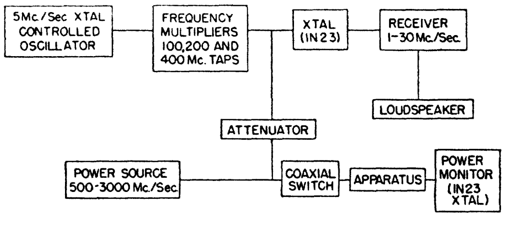

FIG. 32. Circuit for measurement of frequency.

---

[63] J. Lentz and S. Katz, Columbia Radiation Laboratory, Quarterly Report, September, 1947, p. 12.

[64] J. Lentz, private communication.

assuming the value of the anomalous magnetic moment of the electron derived theoretically by Schwinger.[65] Owing to the stability of the permanent magnet, it suffices to make such a calibration rather infrequently as long as the chassis of the rotating search coils is not disturbed. For the most precise work, a calibration is determined on each day of observation.

40. Radiofrequency and Power Measurements

The frequencies used in obtaining the data presented in this paper were near 1600, 2000, 2200, and 2400 Mc/sec, respectively. A 2C39 signal generator was used to produce 1600 and 2000 Mc/sec, and a 2C40 the 2200 and 2400 Mc/sec, although the tube had to be pushed hard to give the required power at the latter frequency. Conventional regulated power supplies are sufficient to give adequate frequency and amplitude stability when the tubes are operated well below their ratings.

The frequency is measured by a beat frequency method as illustrated in Fig. 32, where a signal from the 5-Mc/sec crystal controlled oscillator is multiplied by electronic circuits to 100, 200, or 400 Mc/sec. One of these frequencies is multiplied again by a 1N23 crystal. If the frequency of the signal to be measured is near one of the harmonics, a communications receiver can be used to measure the difference frequency. Care must be taken to avoid one of the false beats due to images, harmonics, and extraneous signals. Nevertheless, this method is quite satisfactory and allows frequency measurements to about 0.01 Mc/sec in the range mentioned. The 5-Mc/sec crystal is standardized against Station WWV.

Rf power supplied to the apparatus is monitored by means of a 1N23 crystal at the end of the transmission line. Although the readings have only a relative significance at any one frequency, they are adequate for the purpose of correcting the data to constant rf power (Sec. 45).

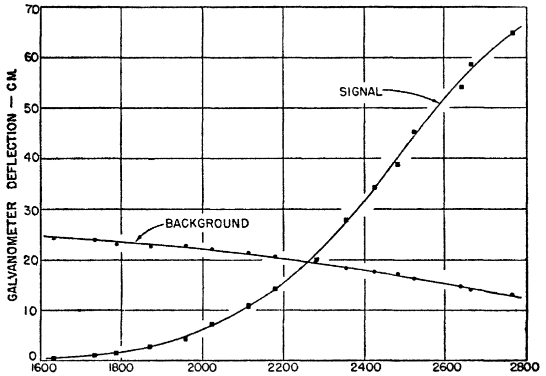

FIG. 33. Dependence on tungsten oven temperature of galvanometer signal due to metastable hydrogen atoms and background deflection due to photo-electrons. The pressure in the source chamber given by Knudsen gauge was approximately constant during the measurements. The signal curve corresponds roughly to that for an oven pressure of 10^{-3} atmos in Fig. 5.

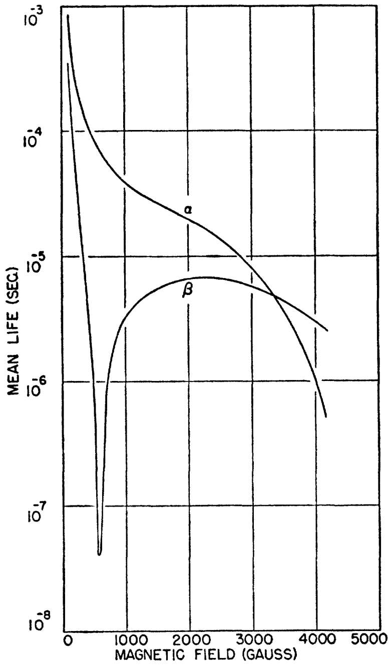

FIG. 34. Theoretical mean lives of metastable states α and β for atoms from source at 2500°K moving perpendicular to a magnetic field. The calculations assume a level shift of 1060 Mc/sec, and neglect quenching other than that due to motional electric field.

G. OPERATION OF THE NEW APPARATUS

41. General Considerations

In taking a resonance curve, typical operating conditions are: source temperature, 2550°K; bombarding voltage, 10.8 v; bombarding current, 200 μamp; gas pressure in the source chamber, 7.5×10^{-4} mm Hg for hydrogen and 5×10^{-4} mm Hg for deuterium; gas pressure in the detector chamber about 3×10^{-5} mm Hg, and some intermediate value in the bombardment chamber. Under these conditions, the signal due to metastable atoms is from 100- to 140-cm galvanometer deflection when the apparatus is considered usable. Fluctuations may amount to a few millimeters on favorable occasions.

Although larger signals can be obtained at higher gas admission rates, it was found that objectionable fluctuations in signal occur when the source chamber pressure is greater than about 8×10^{-4} mm Hg. At equal pressures, deuterium gives about 50 percent more signal than hydrogen. Consequently, although the deuterium working pressure is taken lower than for hydrogen, the signal is steadier, and the data are more accurate.

Similarly, larger signals can be obtained by elevating the temperature of the hydrogen dissociator, as can be seen from Fig. 33. The adopted temperature is one that gives long life of the tungsten tube and fairly large

---

[65] J. Schwinger, Phys. Rev. 76, 790 (1949).

signals without unduly heating the apparatus. In this figure, the curve labelled "background" is about twice as large as would be obtained at present because of some subsequent improvements in the electron gun. The curve labelled "signal" corresponds roughly to the middle curve of Fig. 5.

In contrast to behavior with the apparatus described in Part I, operation of the electron bombarder is only slightly dependent on the magnetic field when it is greater than about 50 gauss. This is presumably due to the much more homogeneous magnetic field in the present apparatus. Nevertheless, the signal due to metastable atoms is still quite dependent on the magnetic field.

As explained in Sec. 16, the motional electric field $\mathbf{E}=(\mathbf{v}/c)\times\mathbf{H}$ causes a quenching of the two metastable states α and β at different rates. The lifetimes of these states may be calculated according to Eq. (42), suitably generalized to allow for the multiplicity of competing states; and the results are shown in Fig. 34.

In addition, there may be quenching due to stray electric fields in the electron bombarder or elsewhere along the beam. These could markedly reduce the magnitude of the signal where there is near degeneracy of the $2^2S_{\frac{1}{2}}$ and $2^2P_{\frac{1}{2}}$ states, which may occur for both α- and β-states at low magnetic fields, and for state β in the vicinity of the crossing point of states β and f in Fig. 14.

Beyond this point, the beam of metastable atoms begins to contain an appreciable fraction of atoms in the lower metastable state. The actual amount is very dependent on the presence of stray electric fields, because of the near degeneracy. Complications which this imposes on the analysis of resonance curves will be considered in Parts III and IV.

42. Excitation Curves for the State $2^2S_{\frac{1}{2}}$

Excitation curves have been very instructive in the study of the relationship of electron bombarder conditions and signal. In addition, they have an intrinsic interest of their own; but unfortunately the present apparatus is not well adapted to taking good excitation curves.

The curves of Fig. 35 labeled "signal" represent the variation of the beam of metastable atoms with electron accelerating voltage, and "background" the corresponding current due to photons. Curves A are taken with the hydrogen dissociator turned on, i.e., for the atomic case, and curves B for the oven at room temperature, i.e., for the molecular case.

The apparent threshold of signal in case A is 9.3 v, which is to be compared to the expected value of 10.2 v. This discrepancy may be attributed to the combined effect of (1) thermionic energy of emission of bombarding electrons, (2) contact potential differences between the tungsten filament and molybdenum anode, (3) reduction of electron energy by space charge, (4) filament voltage drop, (5) recoil dilution factor of Eq. (22) variable with electron bombardment energy, and (6) effects due to charged insulating layers on grid and anode.

Some of these effects contribute merely a constant additive correction to the voltage scale. Thus, (1) should add about $\frac{1}{3}$ v, while (2) should be the difference between the work function between the tungsten filament and molybdenum anode, for clean surfaces $4.5-4.1=0.4$ ev.

The reduction of electron energy due to space charge will in general both distort the excitation curve and change its threshold. If the bombarding current is vanishingly small, the error disappears. In order to be able to use a finite but small current and avoid distortions, the following procedure was adopted. As the nominal energy eV_0 of the electron beam was varied, the bombarding current I was also varied so as to keep the charge density constant. Assuming small space charge, this requires that I and V_0 be related by the equation,

$$IV_0^{-\frac{1}{2}}=\text{const.} \tag{98}$$

In that case, the effective energy eV of the beam would differ by a constant amount from the nominal energy

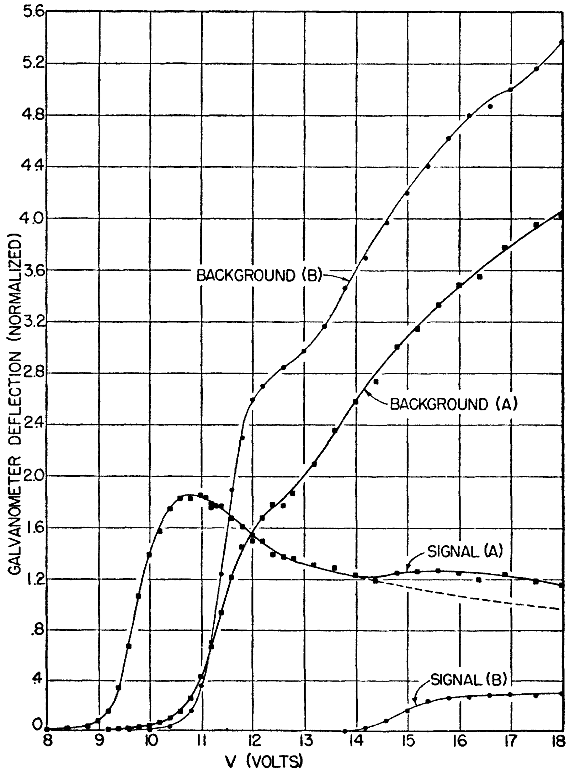

FIG. 35. Excitation curves (for deuterium) giving variations of signal and background with nominal energy of electron bombardment. Curves marked (A) were taken with tungsten oven at 2550°K, while the oven was at room temperature for those marked (B). The curve marked Signal (B) is due to the process of molecular dissociation discussed in Sec. 7, while the hump on Signal (A) starting at 14 ev corresponds to the same process occurring in the molecular gas in the bombardment chamber.

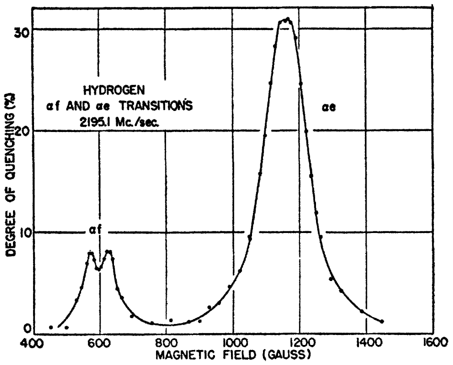

FIG. 36. Observed resonance curves for hydrogen taken at 2195.1 Mc/sec with power chosen to bring the *αe* peak to about 31 percent quenching. The hyperfine structure of the transition *αf* is clearly resolved, and the separation is about as expected in Sec. 17, assuming the hfs of the $2^2P_{\frac{1}{2}}$ states to be $\frac{1}{3}$ of that for $2^2S_{\frac{1}{2}}$. A more quantitative test of this ratio must await accurate curve fitting of such data to a theoretical formula.

eV_0, and effect (3) would simply give an additive constant error in the voltage scale. It is, of course, necessary to reduce the data to constant bombarding current, assuming that when the space charge is small, the signal is proportional to the bombarding current at a given effective energy. According to a result of Nergaard,[62] the depression of the potential in a thin electron beam is given by

$$V_0-V=I/(Cv), \tag{99}$$

where $v=5.93\times10^7V^{\frac{1}{2}}$ is the electron speed and C is the "capacity per unit length" of the electron beam,

$$C=2w[4\pi\cdot\tfrac{1}{2}d\cdot9\times10^{11}]^{-1}, \tag{100}$$

with w the width of the electron beam, and d the distance separating the top and bottom of the U-shaped anode. For $w=1$ cm, $d=0.050$ in$=0.127$ cm,

$$V_0-V=6\times10^3IV^{-\frac{1}{2}}\text{ volt}; \tag{101}$$

and for $I=50\times10^{-6}$ amp, $V_0=10.8$ v, $V-V_0=0.1$ v, so the approximations in Eq. (98) should be good.

The voltage drop (4) has a more important effect. Because the filament is centertapped, and the total voltage drop is about 1.7 v rms, the maximum voltage correction is $\frac{1}{2}\sqrt{2}1.7=1.2$ v peak. Since not all of the filament length is effective in producing electrons, this figure is somewhat high; and one volt will be taken as the correction to be added to the nominal voltage scale.

The variation of recoil dilution factor with energy would not be expected to alter greatly the observed threshold, although it might seriously change the shape of the excitation curve at higher energies.

With the corrections estimated above, $0.3+0.4-0.1+1.0=1.6$ ev, the observed threshold would be $9.3+1.6=10.9$ ev, which is too high by 0.7 ev, according to theory. It cannot be said whether this difference is due to errors in the above estimates, or to item (6) discussed in the next section.

In any case, the apparent threshold energy of signal (*a*) is low by $10.2-9.3=0.9$ ev, so that presumably the apparent threshold energy of signal (*B*) due to dissociation of molecules should be raised by 0.9 ev, giving $14.2+0.9=15.1$ ev in agreement with the expectations of Sec. 7. It is clear that, compared with the adopted method, the molecular dissociation method of producing metastable atoms directly gives a very unfavorable ratio of signal (*B*) to background (*B*) resulting in large fluctuations.

43. Disappearance of the Signal

It was remarked in Sec. 35 that no difficulties with emission poisoning have occurred with the tungsten cathode. However, there has still been considerable difficulty with disappearance of the beam of metastable atoms at various times. If one starts with a clean apparatus having new oil in all the pumps, a month may elapse before the signal becomes unusably small. For a time thereafter, it is possible to regain the signal by heating the anode of the electron bombarder before observations. Subsequently, this does not suffice and it is necessary to heat the anode during the taking of data; and, finally, it becomes impossible to keep a usable signal at all. The remedy in such a situation is to clean the inside of the apparatus thoroughly and replace all of the pump oil.

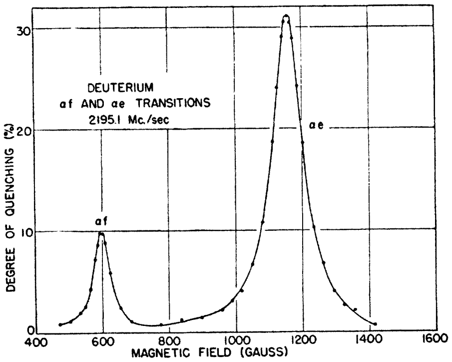

FIG. 37. Observed resonance curves for deuterium taken at 2195.1 Mc/sec with power chosen to bring *αe* peak to about 31 percent. Each peak is the composite of three unresolved peaks separated by about 9 gauss (compared to about 59 gauss for hydrogen).

If the apparatus is in a clean condition, it is observed that as the bombarding current is increased, the signal increases also until a current of about 400 μamp is reached, after which the signal rapidly decreases to a value of only a few centimeters. The background behaves similarly. When the signal has partially disappeared, as described above, the optimum current is less than 100 μamp. At this state, heating the anode will usually restore the optimum current to something like 300 μamp. At later stages this becomes impossible.

The probable explanation of this phenomenon, as already mentioned in Part I. is that the surface of the anode becomes coated with an insulating substance which acquires a negative charge under electron bombardment. When the poisoning has reached the acute stage, brownish-black deposits become visible on the anode in the region where the electron beam strikes. In some cases, the shadow of the grid wires can be seen on the anode. As a result of the action of the crossed magnetic field and electric field resulting from space charge repulsion, the shadow is somewhat skewed. The fact that deposits form in this way is taken as evidence that they are produced by breakdown under electron bombardment of an organic layer on the anode surface. The substance causing these deposits has not been determined; but it is probably a decomposition product of pump oil vapor, apiezon wax, or solvent vapor which is produced by electron bombardment, reaction with atomic hydrogen, or thermal decomposition. The formation of such visible deposits under electron bombardment is well known[66] to workers in electronics, although they are mostly reported at energies of 12 ev or more, whereas only 10.8 ev is used here. Of course, many of the difficulties experienced with the electron bombarder are peculiar to the low energy required for work just above the critical potential of hydrogen.

Another effect noted has been a varying contact potential of about 0 to 0.6 ev in the rf line between the electrostatic quenching electrode and the center conductor. This phenomenon will be discussed in a later paper in another connection. Visible deposits accumulate on the electrodes of the rf line and on the detector target *j*. These are in part related to the deposits in the electron bombarder and also to material evaporated directly from the hydrogen dissociator, possibly an oxide of tungsten.

H. OBSERVATIONS

44. Transitions $\alpha\beta$ $2^2S_{\frac{1}{2}}$ $(m=1/2\rightarrow m=-1/2)$

As mentioned in Sec. 16 and illustrated in Fig. 34, the lower $2^2S_{\frac{1}{2}}$ state β is much less metastable than the upper state α for a considerable range of magnetic fields. Consequently, it should there be possible to observe transitions from α to β, since atoms in the β-state do not reach the detector. The corresponding resonance curves should have a width determined by the reciprocal life of the β-state, and as this is considerably longer than the life of the nonmetastable states such as *e* and *f*, the $\alpha\beta$-resonances should be much narrower than those for transitions αe, αf, etc. Even at the crossing point of levels β and *e*, the life of state β is 4×10^{-8} sec according to Fig. 34, so that the half-width ought to be $1/(2\pi\tau)$ or 4 Mc/sec instead of 100 Mc/sec as for transitions to the more highly damped states.

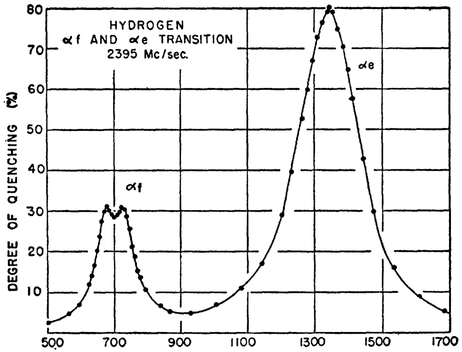

FIG. 38. Observed resonance curves for hydrogen taken at 2395 Mc/sec with power chosen to bring αf peaks to about 31 percent and thereby considerably saturating the αe peak.

Since the frequency of the $\alpha\beta$-transition is closely given by Eq. (97), a very convenient method for determination of magnetic field in the apparatus should be available.

Such resonances were sought with the previous apparatus, but, owing to smallness of signal and lack of constancy and homogeneity of the magnetic field, could not be observed. In the present apparatus, the sharp transitions $\alpha\beta$ are easily observable and are used for magnetic field calibration. Some examples of the $\alpha\beta$-resonances are discussed in Sec. 47.

45. Resonance Curves for Transitions αe and αf

The data of Part I were taken at a large number of frequencies in order to map out the entire field of observable transitions such as is shown in Fig. 25. In the present paper and in those to follow, the plan is to concentrate on obtaining accurate data at only a few frequencies. This procedure is based on the assumption that aside from the presence of the shift of the $2^2S_{\frac{1}{2}}$ state and a possible small change in the doublet separation, the theory of the Zeeman effect is well enough known that the shifts can be calculated accurately from measurements made at a few frequencies. In order to allow for possible deviations from theory, measurements are presented for both the αf and αe transitions of Fig. 15.

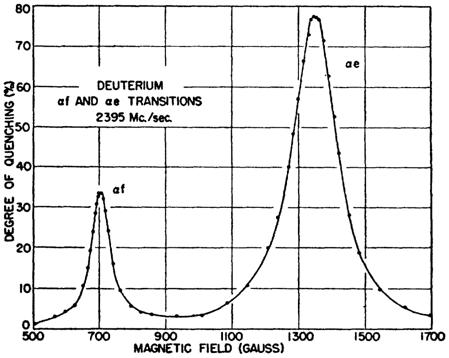

FIG. 39. Observed resonance curves for deuterium taken at 2395 Mc/sec with power chosen to bring αf peak to about 31 percent and thereby considerably saturating the αe peak.

---

[66] C. H. Bachman, *Techniques in Experimental Electronics* (John Wiley and Sons, Inc., New York, 1948).

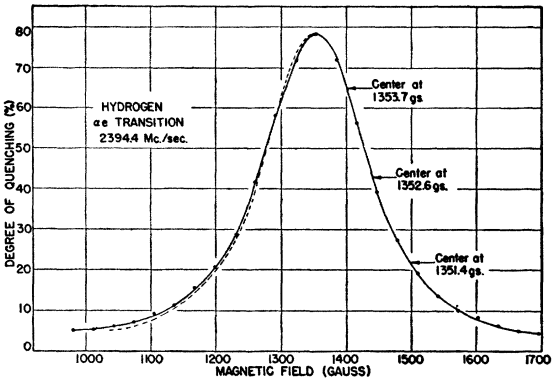

FIG. 40. Detail of αe peak (similar to that shown in Fig. 38) broadened by application of excessive rf power. The dotted curve on the left represents the mirror image of the right side of the resonance curve about an arbitrary magnetic field ordinate. The lack of symmetry is presumably due to causes listed in Sec. 45, but in any case is so small that a fairly reliable level shift can be obtained without elaborate corrections.

On account of the variability of signal with magnetic field discussed in Sec. 41, the resonance curves would be considerably distorted if variations in signal were not taken into account. Consequently, at each magnetic field setting, the signal is measured by quenching essentially all of the metastable atoms by the application of an electric field (Sec. 36). The degree of quenching by the radiofrequency field is then expressed as the percentage of the total possible quenching. This procedure also minimizes distortions due to changes in signal produced by other causes such as changing pressure, bombardment current, drift of hydrogen dissociator temperature, detector efficiency, etc. These quantities are usually only slowly variable, so that the process is quite effective. Changes in rf power are corrected by measuring the change in the degree of quenching corresponding to a small change in crystal current. For small changes in power this is proportional to the change in power and gives a slope $d\phi/dI_x$, where ϕ is the percentage of quenching and I_x is the crystal current. This measurement is usually made at some standard point where the quenching is ϕ_0. Then at some different ϕ, one has, at least for small quenching

$$d\phi/dI_x = (\phi/\phi_0)(d\phi/dI_x)_0. \qquad (102)$$

It is thus possible to correct all of the points to the same rf power level.

Complete resonance curves are shown in Figs. 36–39. The curves of Figs. 36 and 37 for hydrogen and deuterium, respectively, were taken at 2195 Mc/sec with rf powers giving about 31 percent quenching at the αe peak. The αf peaks are weaker than those for αe because of the orientation of the rf electric field. There is a marked improvement of these results over the nearly comparable ones given in Fig. 15 of Part I. The hyperfine structure of the αf peak for hydrogen is clearly resolved as it should be, and the deuterium resonances are noticeably sharper than those for hydrogen owing to the reduced hyperfine structure for deuterium. In Figs. 38 and 39 are shown corresponding results obtained at 2395 Mc/sec with increased rf power so as to bring the peaks αf to 31 percent. The other resonances αe are then somewhat broadened owing to rf saturation effects discussed in Sec. 13.

Some general remarks are required on the possible methods of taking data to determine the resonance magnetic fields. Essentially three methods come into consideration here: (1) determination of the magnetic fields for which the quenching is maximum by a study of the neighborhood of the maxima only, (2) measurements made on the sides of the resonances near points of inflection in order to determine a midpoint, and (3) a fit of an entire resonance curve to a theoretical resonance curve containing the resonance fields as parameters to be determined.

The third method is soundest in principle, but in practice necessitates taking an enormous amount of data which would require greater long term stability of the apparatus than has been obtained. An advantage of this method would be that all kinds of shifts and asymmetries could (or should) be included in the theoretical formula.

The first two methods will give erroneous results if there are uncorrected asymmetries and shifts. Both methods are in error equally if shifts are present, while the first errs less in the case of asymmetries. On the other hand, a really precise determination of the level shifts requires that all asymmetries be understood and allowed for, so that the intrinsically higher accuracy of determination of the midpoint by method (2) has led to its selection over method (1).

Among the factors which can lead to asymmetries and shifts, besides those basic to radiation theory, are the following: (1) overlap of nearby resonances, (2) variation of the matrix element for the transition as the magnetic field is varied (due to breakup of L–S coupling), (3) incomplete Back-Goudsmit effect for the hyperfine components, (4) differential quenching of the hyperfine components by motional electric fields, (5) curvature of the Zeeman energy curves, (6) Stark effect, and (7) presence in the beam of a small fraction of atoms in the β-state. A lengthy program of calculations and measurements is required to allow for all such sources of error, and will form the subject of Parts III and IV. For present purposes, however, it suffices to take a more purely empirical point of view. The resonances are actually highly symmetrical. This has been tested in Fig. 40, in which an excessive amount of power has been used to further broaden the αe resonance, and thereby increase the chance to observe an asymmetry. Despite this, the centers of the curve obtained at different levels of quenching agree quite closely with each other, and also with the center obtained when using much less power.

A further empirical check was made by comparing the centers for the different resonances αe and αf at

2195 and 2395 Mc/sec. On the basis of these experimental tests, and supported by simple estimates of the effect of the errors listed above, we conclude that no corrections are needed to obtain a result with a limit of error of ±5 Mc/sec from the treatment of the data given below.

46. Data and Results

We now turn to a discussion of some data analyzed by the second method above. These measurements were made on runs of generally high caliber, but certain refinements to be described in the later papers were not included. One defect was that the field calibration made at 2395 Mc/sec was not corrected for motional Stark effect. In order to minimize the effects of uncontrolled changes in search coil calibration, crystal sensitivity, etc., points were taken on alternate sides of the curve in a zigzag fashion, so that the center of the curve could be determined at various levels of the curve. This was done graphically on a large scale plot by reflecting one side about a line of ordinates near the center of the peak. Five or six pairs of points were usually selected along the sides of the curve. Each pair of points permits a determination of the shift. The shift is determined on the basis of the theory given in Sec. 15, using in particular, Eqs. (39)–(41).

In the case of the αf peaks, a rough correction for overlap by the αe resonance was made.

The results for the $2^2S_{\frac{1}{2}}$ level shift in hydrogen from these runs are presented in the form of a histogram in Fig. 41, in which the nominal internal scatter and discrepancy between results for αe and αf give results ranging from 1061 to 1065 Mc/sec. It should be recalled that in using the formulas of Sec. 15, no account is taken of the anomalous magnetic moment of the electron, reduced mass effects, and other corrections mentioned in Sec. 45. In addition, there is a possible error of a megacycle or so in using the $\alpha\beta$-resonance at 2395 Mc/sec for magnetic field calibration without correction for Stark effect. With these possibilities for error in mind, the value for the shift was reported[60] in January, 1949, as 1062±5 Mc/sec with confidence that the finally obtained value would not lie outside this range. Results for deuterium lie in the same range.

47. Observation of Sharp Resonances

As explained in Sec. 39, the sharp transitions $\alpha\beta$ were used to calibrate the magnetic field. These have a markedly different character depending on whether or not the level β is separated from competing levels by their radiation width. An example of the first type, taken at 1995 Mc/sec, is given in Fig. 42, and some of the second type are shown in Figs. 43 and 44. The resonances of the second type are superposed on the broad resonance αe, as shown in Fig. 45.

One of the sharp resonances is observed for each hyperfine state: two for hydrogen and three for deuterium. A peculiar feature of these transitions is that the quenching is *reduced* when the resonance condition $\omega=\omega_{\alpha\beta}$ is satisfied. In the first type of resonance, this reduction occurs at the minimum on the right of the peak. The maximum is located essentially at the field to be expected if motional Stark effect shifting of the levels is considered. In the second type, the quenching of each hyperfine component is also reduced to a small value when $\omega=\omega_{\alpha\beta}$. The width of the resonance corresponds to the lifetime of the β-state at the crossing point of β and e as explained in Sec. 44.

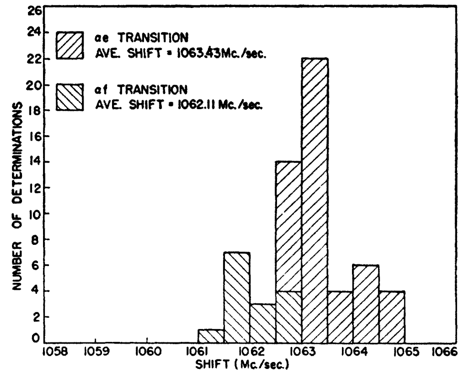

FIG. 41. Histogram showing distribution of results obtained from 61 determinations of $2^2S_{\frac{1}{2}}$ level shift. The difference between results obtained from αe and αf would presumably be removed if the corrections for the errors listed in Sec. 45 were applied. The finally determined level shift may be expected to lie in the range 1062±5 Mc/sec.

The theory of these transitions leads to an understanding of the above features. It is rather complicated and will be postponed to Part III. However, one can obtain a physical picture of the process in terms of an electrical analogy with the problem of two coupled resonant circuits shown in Fig. 46, consisting of a primary with parameters L_1, C_1, R_1 and a lossless secondary L_2, C_2 coupled to the first by a mutual in-

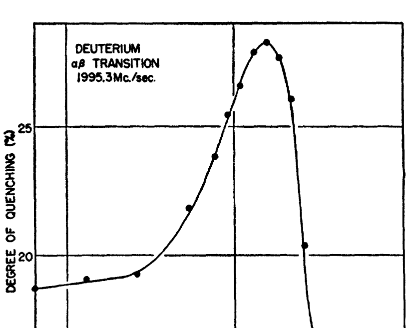

FIG. 42. Example of $\alpha\beta$-transition taken at 1995.3 Mc/sec. The peak shown is the center one of three observed with deuterium separated by about 9 gauss. For hydrogen, two peaks separated by about 63 gauss would be observed. The resonance fields for transitions αf and αe at this frequency would be 490 and 970 gauss, respectively.

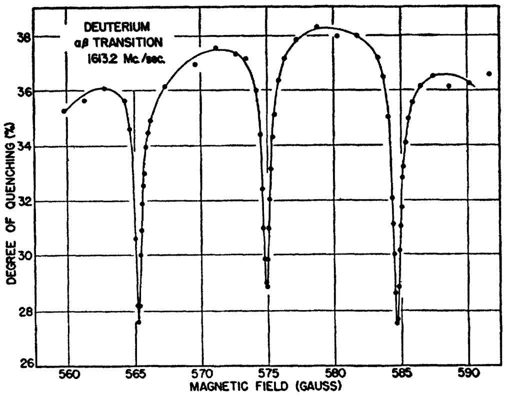

FIG. 43. Sharp resonance curves for transitions $\alpha\beta$ in deuterium at a frequency 1613.2 Mc/sec, for which the broad resonance αe overlaps the sharp resonance $\alpha\beta$.

ductance M. The resonance frequency $\omega_1=(L_1C_1)^{-\frac{1}{2}}$ of the first circuit corresponds to the transition from α to e, and radiation damping is represented by the resistive element R_1. The resonance $\omega_2=(L_2C_2)^{-\frac{1}{2}}$ of the second circuit occurs at the frequency of the transition $\alpha\beta$. As represented by setting $R_2=0$, the β-state does not decay directly. There is no direct coupling from α to β (except by relatively unimportant magnetic dipole radiation), while in the electrical circuit analogy, the second resonator is excited only indirectly by its mutual inductive coupling to the first circuit. In the atomic case, the motional Stark effect provides the coupling between β and e. The input admittance of such a circuit (and hence the power absorbed) has a broad resonance for $\omega=\omega_{\alpha e}$, while in a very narrow band about $\omega=\omega_{\alpha\beta}$ the reflected impedance of the lossless secondary is large and reduces the response of the network.

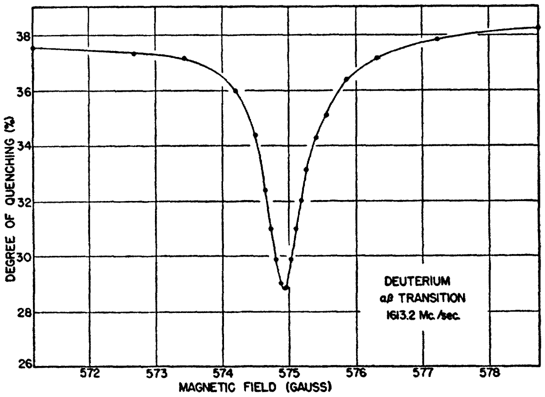

FIG. 44. Detail of the central peak shown in Fig. 43 obtained in another measurement.

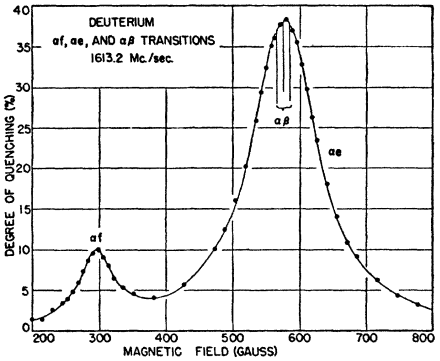

FIG. 45. Panoramic view of resonances αf and αe in deuterium at 1613.2 Mc/sec showing location and magnitude of sharp resonances of Fig. 43.

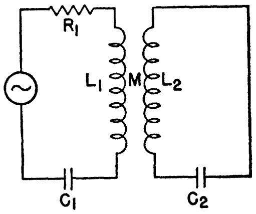

FIG. 46. Electrical circuit analog for interference of transitions αe and $\alpha\beta$.

The authors have benefited greatly from the cooperation and assistance of Messrs. N. T. Williams, P. F. Yergin, and J. J. Lentz as well as others mentioned in Part I.